NDT&E International 142 (2024) 103002

Contents lists available at ScienceDirect

NDT and E International

journal homepage: www.elsevier.com/locate/ndteint

Material-enabled damage inspection of multifunctional shape memory alloy tufted composite T-joints

WeeLiam Khor [a], Anil R. Ravindran [b], Raj B. Ladani [b], Manatsawee Limprapuwiwattana [b], Pete Whitton [c], Charlotte Meeks [d], Andrew D. Foreman [d], Francesco Ciampa [a,*]

[a] School of Mechanical Engineering Sciences, University of Surrey, Guildford, GU2 7XH, United Kingdom
[b] School of Engineering, RMIT University, Melbourne, 3000, Australia
[c] National Composites Centre, Bristol & Bath Science Park, Emersons Green, Bristol, BS16 7FS, United Kingdom
[d] Applied Science, QinetiQ, Farnborough, GU14 0LX, United Kingdom

ARTICLE INFO

Keywords:
DIC
Material enabled thermography
Damage detection
Shape memory alloys

ABSTRACT

The through-the-thickness reinforcement of carbon-epoxy composite joints with shape memory alloy (SMA) tufts has shown significant improvement of the mechanical strength, fracture toughness, and delamination resistance. This study explores the thermal-electric properties of SMA filaments tufted in composite T-joints to exhibit multiple functionalities including material-enabled thermographic inspection and structural health monitoring via *in-situ* strain sensing. Infrared thermography image analysis was performed on both pristine and damaged T-joint specimens subject to pull-off testing. Experimental results showed that the heat generated by SMA tufts measured by an infrared camera provided accurate indication of delamination perpendicular to the tuft direction. SMA tufts were also used as strain sensors embedded within the T-joint. Local changes of the electrical resistance in SMA filaments, both separately and within the joint, were observed during pulling loads. Digital Image Correlation measurements exhibited good correlation between electrical resistance variations and the opening of delamination. These results pave the way for the development of multifunctional composite joining systems combining enhanced through-the-thickness damage tolerance and self-sensing capabilities.

1. Introduction

Fibre reinforced polymer (FRP) composites can be designed to exhibit superior mechanical properties in the desired loading direction. However, one common downside is that fibres are aligned in a two-dimensional (2D) plane, leading to a weak plane parallel to the fibres' one. Such weak plane typically fails by delamination since the inter-laminar fracture toughness is significantly lower than the pultruded fracture toughness [1–4]. Additionally, FRP composite designers must rely on mass and cost limiting joining approaches in structural and safety critical applications, which yield increased mass and costs. Mechanical fastening and adhesive bonding are the two mostly used techniques to join thermosetting FRP composites [5]. However, fastening involves the use of rivets, screws and bolts requiring specialised operators and fabrication processes that can increase weight and affect structural integrity (e.g., drilling holes may cause delamination and debonds). Adhesives are relatively weak compared to the bulk composite material and are susceptible to cracking and environmental deterioration in operating environments.

Therefore, alternative joining solutions based on through-the-thickness reinforcement (TTR) technologies have been developed in recent years to reinforce structural FRP composite joints and create a mechanical link between different plies of the composite laminate. In TTR methods, the reinforcement is introduced in the form of fibres, filaments, or rods, positioned in an orientation normal to the laminate plane, which have led to diverse TTR technologies such as three-dimensional (3D) weaving, stitching, z-anchoring tufting and z-pinning [6–8]. All these methods have shown significant improvement in mechanical properties, i.e., the interlaminar fracture toughness and delamination resistance, whilst preserving the laminate's in-plane

Abbreviations: DIC, Digital image correlation; NCF, Non-crimp fabric; R_i, easured resistance, Ω; R_0, Initially measured resistance from the test, Ω; SMA, Shape memory alloy; ΔT, Heat signal due to heating, °C; T_0, Average temperature for the first 250 heating frames, °C; T_h, Average temperature for the first 250 frames before heating, °C; t, Time, s.

* Corresponding author.
E-mail address: f.ciampa@surrey.ac.uk (F. Ciampa).

https://doi.org/10.1016/j.ndteint.2023.103002
Received 15 July 2023; Received in revised form 6 October 2023; Accepted 20 November 2023
Available online 23 November 2023

strength. Among TTR techniques, tufting is one of the most promising since it involves the insertion of the yarn through the layers of a laid-up dry fabric preform via a single needle using automated manufacturing systems with robotic manipulators [9–11]. Unlike stitching, tufting requires access only from a single side of the preform, thus considerably simplifying the manufacturing complexity of the composite joint. Extensive work carried on tufted FRP composites in recent years has shown that the efficiency and effectiveness of tufting is governed by the thread material [12]. Whilst aramid and carbon threads are the easiest option in terms of manufacturing, they are susceptible to environmental degradation and suffer from robustness problems during the tufting process [10,13]. Lombetti and Skodos [14] used metal (copper and steel) threads tufted into composites to achieve significant improvement of delamination and debonding resistance. Several researchers successfully used shape memory alloy (SMA) filaments as the tufting thread for FRP composites [15,16]. SMAs are metal alloys typically made of nickel and titanium that present two unique thermo-mechanical properties, i.e., the "superelastic behaviour" in the austenitic phase and the "shape memory effect" upon heating from a deformed martensitic state [17]. The first property allows SMAs to be completely deformable at room temperature and then, capable of returning to the original shape when the stress is released. This feature enables SMA filaments, when tufted into composite joints, to absorb and dissipate energy during applied loads, thus enhancing the damage resistance of the joint. The shape memory effect allows SMA wires that are heated (e.g., via electrical current through the resistive Joule effect) to exert large recovery stresses up to 800 MPa [18,19]. Ciampa et al. [20] have recently demonstrated that it is experimentally possible to achieve a structurally enhanced multifunctional SMA tufted composites by exploiting the high mechanical, electrical and thermal properties of SMAs. This study showed that thin and flexible SMA filaments (0.13 in diameter) could be directly inserted into carbon/epoxy plate-like composites before resin infusion using a rapid and automated tufting process. Due to the high stiffness and strength of SMAs, a dramatic enhancement in the fracture toughness of SMA tufted composites under Mode I failure (i.e., 8-fold improvement in the G_{Ic} parameter against untufted samples) and Mode II failure via double cantilever beam (DCB) and edge notched failure three-point bending tests, respectively, was achieved. Moreover, post-fracture DCB tests with Digital Image Correlation (DIC) cameras were performed to analyse the "crack-closure" feature of SMA wires through their "shape-memory" effect. By applying a small amount of electrical current to SMA filaments (~1.1 Amp), the generated heat (under 50 °C, which is well below the glass transition temperature of the epoxy resin) successfully activated SMAs and caused the internal crack to shrink from 1 to 0.5 mm. The same authors have also recently demonstrated that it is feasible to manufacture SMA tufted carbon/epoxy T-joints with enhanced ultimate strength and energy absorption under pull-off tests [21].

Electrically conductive materials generally react to strain by exhibiting a change in the electrical resistance [22]. This approach is commonly used in strain gauges, where resistance variations measured from the strain gauge are directly correlated to strain measurements. A number of researchers have shown promising results for applications in wearable technologies [23–26] and sensing for structural health monitoring [27,28]. Several studies have also revealed a good correlation between mechanical strain and electrical resistance changes in stretched SMA wires [29–31], thus suggesting that this material can be embedded within FRP composites to behave as *in-situ* strain sensor for online damage monitoring [32], instead of externally mounted sensors [33]. Additionally, as mentioned above, electrical current can be introduced into SMA wires embedded in the composites to induce heat via the resistive Joule effect, thus facilitating material-enabled infrared (IR) thermography [32,34]. Active IR thermography generally requires surface external heating, volumetric heating (even external heating across the whole specimen volume), or abnormal/selective heating (heating of specific spots in the material) to visualise cracks and delamination in FRP composites using an IR camera [35–37]. For example, Badghaish and Fleming used step-heating IR thermography to detect internal damage in FRP materials by applying heat to the material for a short period of time using optical heaters [38]. IR thermography currently uses high power excitation sources (e.g., flash lamps) to illuminate the sample on its surface and generate heat to detect cracks in the bulk material [39–44]. However, major problems arise when the defect is too deep to be reached by a significant amount of heat, so that the use of external thermal sources may limit the detection of defects only within a few millimetres from the material surface. Moreover, two or more lamps are usually needed to avoid non-uniform heating, thus significantly increasing equipment costs and complexity. Material-enabled thermography have shown to overcome these limitations by using the resistive heating of SMA wires as the internal thermal source for thermographic material inspection [34,45–47].

This paper builds on the recent work carried out by Khor et al. [21] and aims at exploring novel material-enabled multifunctionalities of SMAs tufted in FRP composite T-joints. Particularly, two main functionalities are the focus of this paper, which include (a) the capability of SMA to act as *in-situ* strain sensors for structural health monitoring and (b) to generate internal heat for material-enabled IR thermography. Section 2 reports the manufacturing procedure for the fabrication of SMA tufted T-joint specimens, as well as the experimental set-up for material-enabled strain sensing during pull-off tests and IR thermography. Section 3 illustrates the strain-sensing and thermographic results for the detection of delamination, including the optical fractography analysis for the T-joint specimens. This sections also reports on the change in electrical resistance of the SMA wire when subject to tensile loads. Conclusions are finally reported in Section 4.

2. Methodology

2.1. Materials

T-joints were fabricated using carbon-epoxy composite laminates. The carbon fibre pre-form was made of carbon 0°/90° biaxial non-crimp fabric (NCF), with additional toughener veils and a powder binder. Full details of the composition of the NCF fabric are provided in Table 1 and in Khor et al. [21].

All T-joints were manufactured using the same fibre lay-up with three plies used for each web side and the skin. A noodle filler consisting of a braided unidirectional (UD) cord was used to fill the void in the centre of the T-joint. Preforms were hot debulked at 120 °C for 1 h each to reduce bulk prior to tufting and ease preparation for infusion. Carbon preforms were infused with Hexcel RTM 6-2, a two-part aerospace grade epoxy resin, with an operating temperature of up to 120 °C. Each preform was placed in a three-part resin transfer moulding (RTM) infusion tool, consisting of a base plate and corner pieces to form the T-geometry as shown in Fig. 1. The resin was cured for 2 h at 180 °C once the tooling reached this temperature.

Both plain and SMA tufted T-joints were manufactured, with the latter including SMA filaments tufted in the region between the flange and skin of the specimen. Prior to infusion, 0.13 mm diameter nickel-titanium SMA tufts with an austenite finish temperature below 0 °C

Table 1
- Composition of NCF fabric used to manufacture T-joints.

	Layer	NCF Material	Areal Weight (g/m^2)
5	Powder Binder	Solvay Cycom 7720	10
4	Toughening Veil	TA1903	4
3	Fibre	Tenax-E ITS55 E23 24 K 1600tex, 90°	268
2	Toughening Veil	TA1903	4
1	Fibre	Tenax-E ITS55 E23 24 K 1600tex, 0°	268

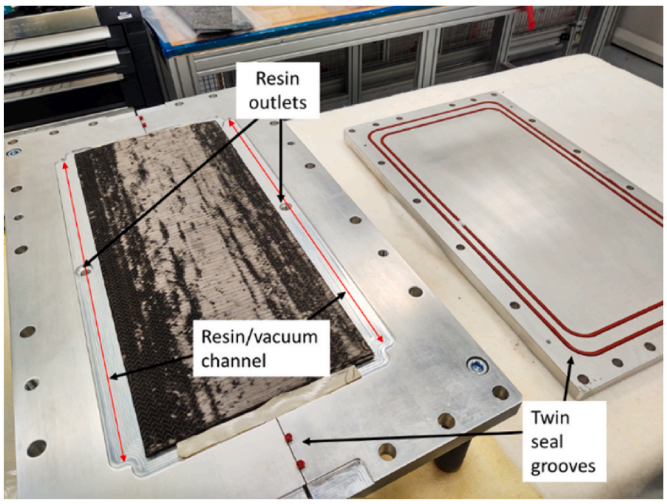

Fig. 1. Infusion tooling with preform inserted.

were inserted using a KSL RS 522 tufting head attached to a Kuka KR240 robot. The nitinol alloy undergoes a phase change from austenite to stressed martensite when deformed by ~8% strain (note the precise alloy composition and heat treatment of the nitinol is proprietary information) [21]. This process was carried out with the preform held in specific tooling, with tufts entering from the skin side and looping on the web side of the T-joint. T-joint coupons with 3.44 mm (high density), 4.3 mm (intermediate density) and 5.16 mm (low density) square tuft interspacing were produced, consisting of parallel tuft rows, with equal spacing between rows and each tuft in a row. The internal and external diameters of the tufting needle were 1 mm and 2.3 mm, respectively. The tufted rows were 25 mm wide and filled the area where the web and skin were in contact either side. Tuft loops were kept short (~2 mm) to ensure no interference between tuft rows. An un-cut tufted section with 3.44 mm high density spacing is shown in Fig. 2.

T-joint sections were cut out using a Sharp & Tappin panel saw. For tufted sections, leads on the start and end of each tuft row were preserved and extracted from the resin surface to allow connection for strain measurement and resistive Joule heating.

2.2. Mechanical pull-off tests of T-joints

As shown in Fig. 3, T-joints were clamped on the skin, whilst the web

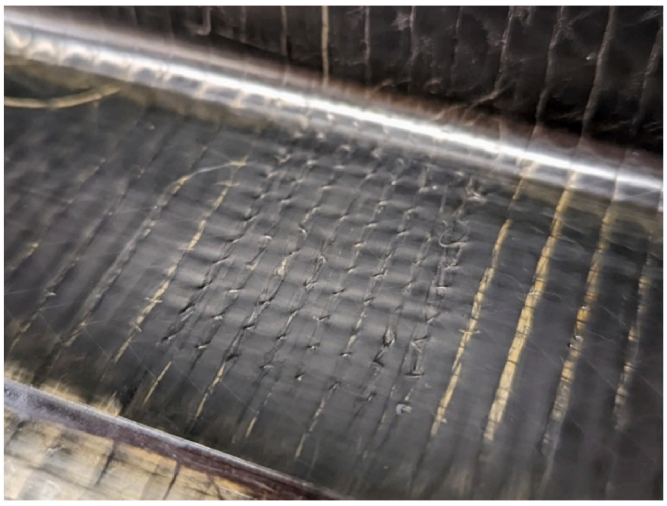

Fig. 2. Illustration of 3.44 mm spaced tufting on the carbon-epoxy composite T-joint.

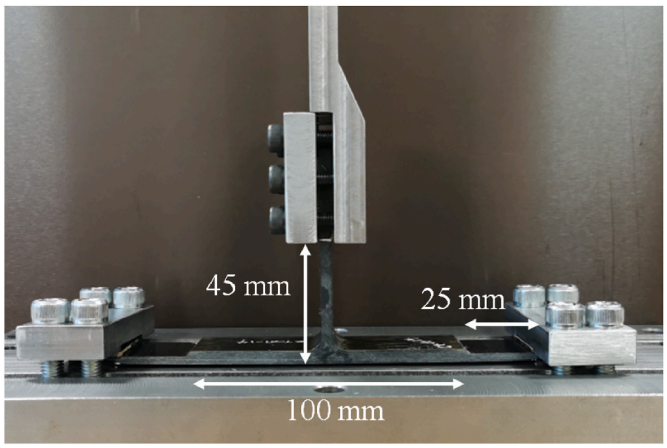

Fig. 3. T-joint specimen pull-off test configuration.

was pulled axially. The web, skin-flange and skin regions were 4.6 mm, 5.5 mm and 3.3 mm respectively, whilst the width of each specimen was 30 mm. Monotonic axial loading was set at 1 mm/min.

Digital image correlation (DIC) was applied on the surface of the specimen to measure the displacement field during the loading and delamination process. Black matt paint was used as background with white speckles. A pair of 9 MP Manta G-917B ASG cameras was set up with commercial VIC-3D DIC analysis software by Correlated Solutions for the analysis of surface measurements (Fig. 4).

It should be noted that a thorough analysis of the mechanical behaviour of SMA-tufted composite T-joints subject to pull-off tests by varying tuft densities was performed by the same authors to analyse the mechanical failure between the flange and the skin, with results reported in Ref. [21]. The same tuft spacing used in this work was investigated, i.e., 5.16 mm (low density), 4.3 mm (intermediate density) and 3.44 mm (high density), with SMAs tufted on the flange side of the skin-flange interface of the T-joint. Mechanical testing results revealed a significant improvement of the mechanical performance of SMA tufted composites against T-joint samples with no tufts, with an increase of up to 110% in strength and 450% in absorbed energy capacity using high density SMA tufts.

Fig. 4. DIC setup and mechanical testing configuration.

2.3. In-situ strain sensing of SMA tufts

Two experimental approaches were adopted for strain sensing, i.e., single wire sensing acquisition using a multimeter (Keithley 2110 5 ½ digital multimeter), and multiple wire simultaneous measurements using Arduino Mega (Fig. 5). Both approaches consisted of measuring the resistance of SMA wires whilst the T-joint specimen is axially loaded. In the single wire resistance measurement, the SMA in channel 1 (Fig. 6) was measured using a multimeter while the T-joint was loaded. In the multiple wire measurements, instead, the Arduino Mega was connected to two HX711 load cell amplifier with a Wheatstone bridge configuration. Digital values measured from Arduino were calibrated using fixed resistors of known resistance. For the multiple wire testing, the resistance of SMA wires in channels 1 and 2 were simultaneously measured using the Arduino system (Fig. 6).

2.3.1. In-situ tensile test and strain sensing of the single SMA wire

A four-probe electrical measurement technique was performed to measure the change in DC electrical resistance as the single 0.13 mm diameter SMA wire was subject to tensile load, as illustrated in Fig. 7. Tensile tests were performed at displacement control at a rate of 0.25 mm/min using Zwick/Roelle Z010 universal testing machine where the load and displacement values were recorded. Three samples were tested and had a gauge region of 25 mm. Before conductivity testing, the filament ends (15 mm long on each end) were coated with conductive silver paste (supplied by RS Component Ltd.) and then soldered on electrical leads which were wrapped with electrical insulating tape to allow for proper placement on the test fixture. The electrical leads were then connected to a Keysight micro-Ohmmeter (Keysight Type 3442OA), as shown in Fig. 7. The test protocol was directly adapted from Ref. [48]. During tensile tests, DC electrical resistance measurements were recorded concurrently.

2.4. Material-enabled IR thermography

A high performance FLIR A6780 series IR camera with 3 MP resolution at 62.5 frame per second was used to record apparent temperature signals emitted by the SMA tufts from the bottom of the specimen. This configuration was used to mimic the practical detection approach in a real structure, where the web is pointing towards the inside of the structure for support or stiffening purposes, whilst the bottom of the specimen represents the outer surface accessible to the technical operator. Thermographic observation was performed on both damaged and undamaged specimens. The undamaged specimen was used as the baseline for comparison purposes, thus enabling a better identification of the heat signal due to delamination in the damaged sample.

A 30 V 2 A power supply unit (TTi EL302T triple power supply unit) was used to provide constant electrical current to the system to generate resistive Joule heating. Electrical current was calibrated with a potentiometer in series, and it was applied across the SMA to heat up the composite tufted T-joint (Fig. 8). A step heating approach was used to

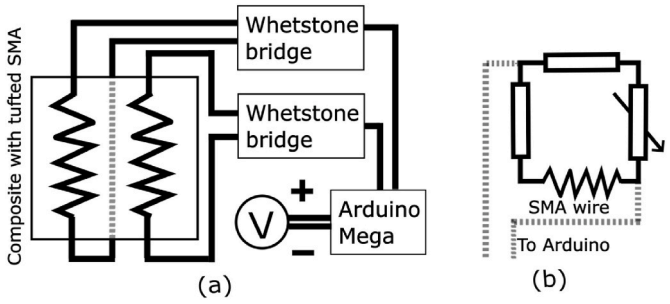

Fig. 5. Schematic of the circuit diagram for multi wire simultaneous resistance measurements (a), and the configuration of the whetstone bridge (b).

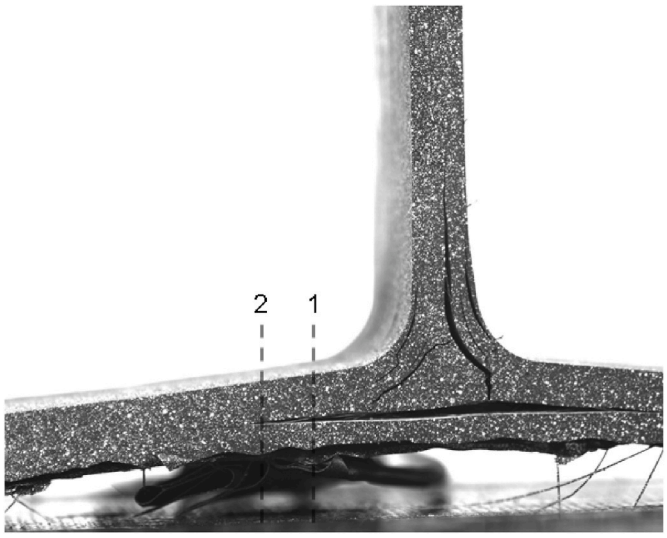

Fig. 6. Position of channels 1 and 2 connected to SMAs used to measure variations of the resistance during axial pull-off tests.

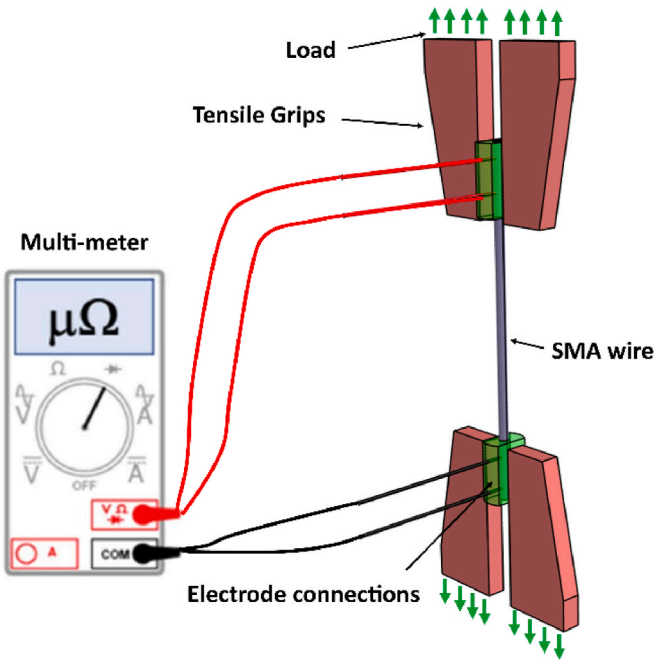

Fig. 7. Schematic of the in-situ tensile test and electrical resistivity measurements setup.

record the heat signal from the IR camera. Specifically, the specimen was recorded without any current input for 3 s, followed by constant current introduction (heating) for additional 3 s, and the final 4 s without current to cool down. Similar approach have been employed successfully by Pinto et al. [34]. For the thermal analysis, background subtraction was initially applied to the raw thermal data. The measured apparent temperature contrast, ΔT, was calculated as follows,

$$\Delta T = T_h - T_0, \tag{1}$$

where T_h is the average temperature for the first 50 frames when current was introduced into the specimen, and T_0 is the average for the 50 frames before heating of the SMA wire. This process removes the background average and fluctuations in the thermal signals. Moreover, data post-processing using Principal Component Analysis (PCA) was

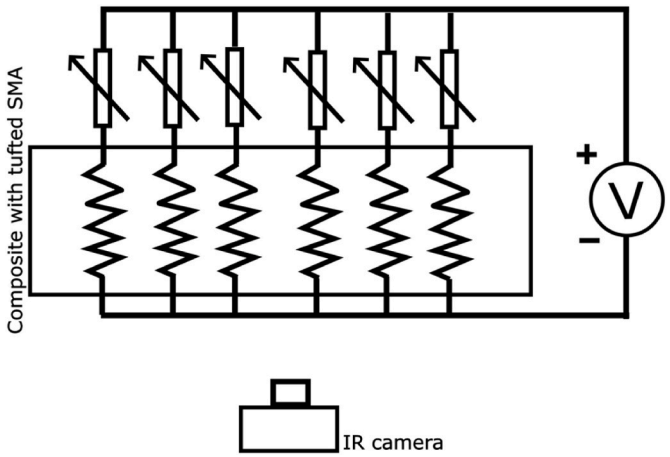

Fig. 8. - Circuit diagram for the calibration of SMA wires in material-enabled IR thermography.

used using Matlab software to assess apparent temperature changes at the pixel level. A thorough mathematical formulation of PCA for defect detection in composites using IR thermography is reported, for example, in Wang et al.'s paper [49]. PCA allows the extraction of principal component coefficients that are used to enhance defect visualisation in thermal images [50,51]. The first principal component was here used to reshape the image, while the mean of images was subtracted to spot thermal variations related to the damage signature. This process highlighted pixel level variations in the thermal intensity dissipated by composite specimens during the heating and cooling steps. Three different combinations were used for PCA to highlight observations in the unheated, heated and cooled composite:

- Five unheated image
- Five unheated image + one heating image
- Five unheated image + one cooling image

3. Results and discussion

3.1. Load-displacement results from pull-off tests

Load-displacement curves from the plain and tufted specimens are illustrated in Fig. 9. The specimens reinforced with SMA tufts showed significant improvement in mechanical properties, particularly on the maximum load. Similarly, the tufted composite showed up to 435% increase in energy absorbed at maximum load compared to the plain composite. However, as also remarked in Khor et al. [21], damage initiation load and specimen compliance were similar for both plain and reinforced composite specimens, as there is no reinforcement in the damage initiation area (noodle region) of the tufted specimen.

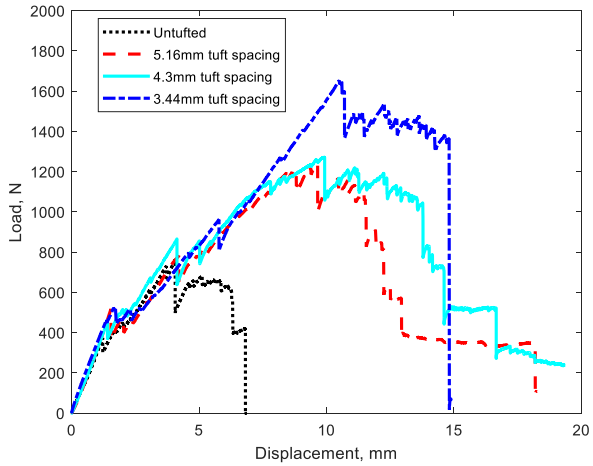

Fig. 9. - Load-displacement trace from the T-joints: plain, 5.16 mm, 4.3 mm and 3.44 mm tuft densities.

3.2. Strain sensing results

Fig. 10(a) shows the electrical resistance and the corresponding delamination opening from a 5.16 mm tuft spacing T-joint specimen. The electrical resistance was measured from the SMA tuft in channel 1 (Fig. 6) using a multimeter as the T-joint was continuously loaded with increasing time. The delamination opening displacement was measured using the DIC system. The resistance recording shows a minimal variation up to $t \approx 450$ s, followed by a rapid increase in electrical resistance, spikes and fluctuations. In contrary, the delamination opening remains constant from the start of the test, increasing with a general increasing gradient from $t \approx 250$ s. Magnifying measurements for $t < 450$ s [Fig. 10 (b)], the resistance plot depicts low magnitude fluctuations up to $t \approx 270$ s. This is likely due to the rigid movement of the specimen during loading and minor changes in the local stress state of the SMA tuft. In the time region between 270 s $< t <$ 450 s, an increasing trend in the measured resistance is observed due to the elastic deformation of the SMA occurring during loading, before a large spike occurs at $t \approx 450$ s as

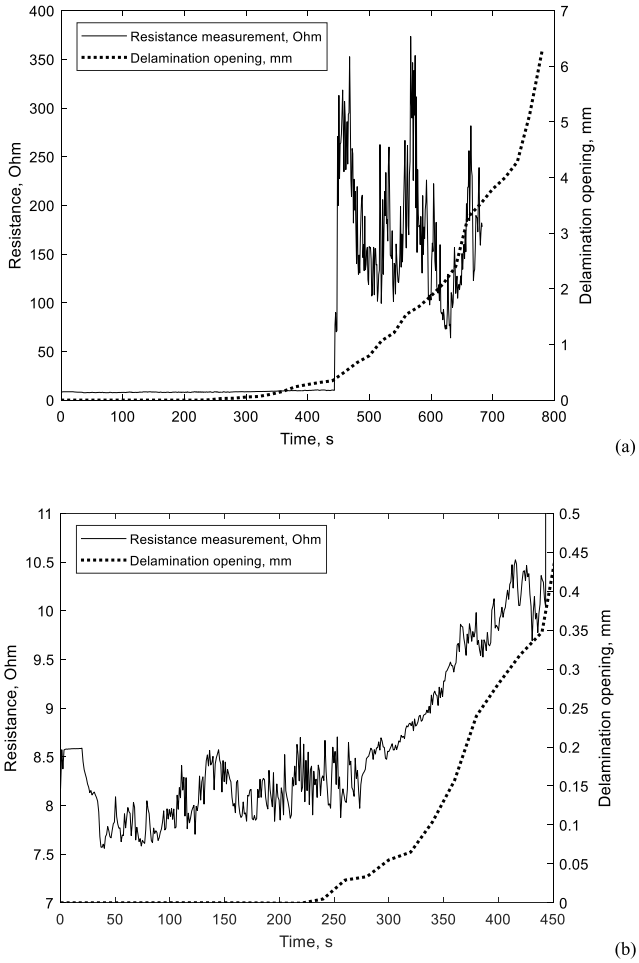

Fig. 10. The resistance and delamination opening displacement measured from the SMA tuft as the specimen is loaded: (a) full test, and (b) magnification for $t < 450$ s.

mentioned above.

The resistance-delamination measurement test was carried out with 4.3 mm and 5.16 mm tuft spacing specimens. Resistance measurements were normalized to the initially measured resistance, R_i/R_0 and synchronized to the displacement measurement obtained from the DIC, as shown in Fig. 11. Excluding data fluctuations at initial stages of the opening displacement and after the rapid increase of resistance, a good linear relationship was found between the resistance and the delamination opening displacement. Such a good correlation of the elongation-resistance appeared to be independent of the tuft spacing used to manufacture T-joint and it was similar to other SMA strain-resistance studies reported in literature [29,31].

Focusing on the 4.3 mm tuft spacing specimen, the moving average of multiple point resistance measurements obtained from the Arduino system was converted to the corresponding delamination opening based on the correlation in Fig. 11 and plotted with increasing specimen displacement (Fig. 12). The SMA wire closest to the web (i.e., Channel 1 in Fig. 6) indicates delamination at around 4.5 mm specimen displacement, followed by the adjacent wire (Channel 2) at about 5.2 mm specimen displacement. Visual observation of the crack tip initiation at both positions was performed by tracking the image files. The visual crack tip initiation tends to occur before changes were observed from the SMA wire signals. This is mainly due to the minimal active length of SMA being strained during crack tip initiation in hairline cracks.

In-situ relative resistance and tensile test results of the single SMA wire in isolation are presented in Fig. 13. The stress versus strain response of the single SMA wire is consistent to previous reports on the tensile properties of SMA wires [16,17], which exhibits a pseudo-elastic response indicative of the phase change from Austenite to twinned Martensite to Martensite. With increase in strain within the Austenitic phase (see Fig. 13), the relative resistance change increases with strain. However, with the onset of austenite to martensitic phase, the relative resistance change decreases significantly then reach a steady-steady state value upon approaching the Martensitic phase. Upon fracture of the SMA wire, there is a sudden increase in the relative change. This correlate well with findings shown in Fig. 10, where a sudden decrease in the relative resistance change occurs with the increase in crack opening displacement for the T-joint. However, it is important to note that the SMA are not electrically isolated from neighbouring tufts, which may correlate to noise observed in Fig. 10(a). Previous studies by Vaijapurkar and Ravinder [52] have also shown that the electrical resistance of an SMA was dependant on the crystalline phase of an SMA wire. For the present study, this demonstrates the potential of using SMA wire for in-situ NDT and damage detection for determining degree of crack opening within a composite laminate.

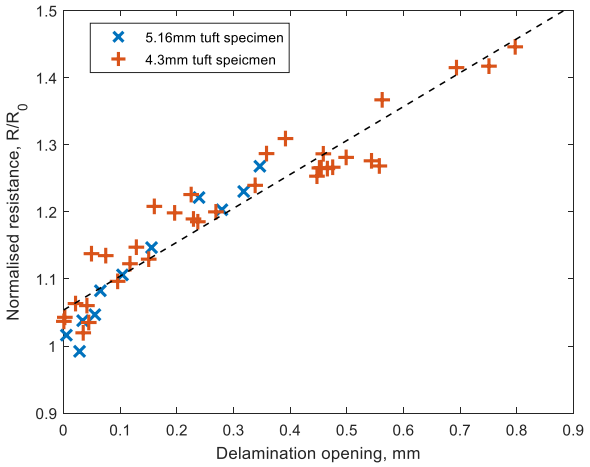

Fig. 11. Correlation between the normalized resistance, R/R_0 and the delamination opening displacement.

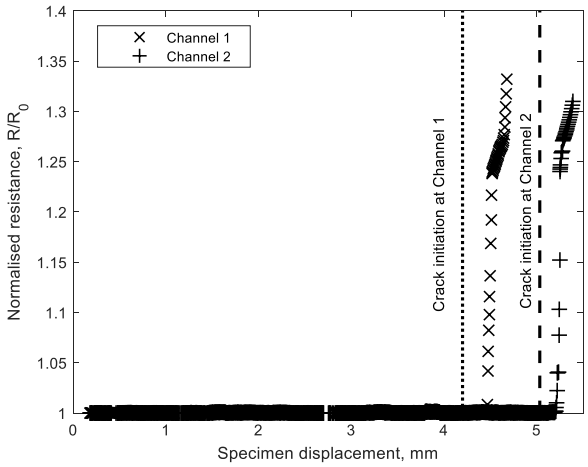

Fig. 12. Estimation of delamination opening displacement at the SMA wire tuft position for the corresponding specimen displacement.

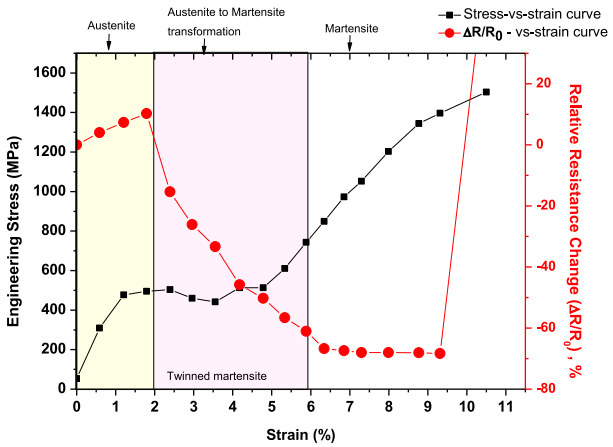

Fig. 13. Experimentally measured relative resistance change and tensile stress-strain measurements of the single isolated SMA wire.

3.3. Material-enabled thermographic results

The temperature contrast, ΔT, from Eq. (1) was extracted during the heating and cooling phases of the composite. Four levels of electrical current were applied to each SMA wire, i.e., 0.33 A, 0.25 A, 0.2 A and 0.1 A. As wires thread across the composite in the vertical direction, thermal data in the vertical direction was averaged to facilitate visualisation in a 2D plot. For the heating step, the temperature difference measured from the undamaged T-joint specimen was plotted in Fig. 14 against the corresponding horizontal pixel position. In the undamaged specimen, peaks indicate the positions of the SMA tufts within the composite. Through the resistive Joule effect, wires generated higher apparent temperature peaks with the increase of current input, similar to what has been observed in literature [34]. These peaks are mainly due to the electrical energy input into the wire.

On the same undamaged SMA tufted T-joint specimen, the temperature difference was observed on the heating and cooling step of a single wire at 0.25 A (Fig. 15). A significant difference in the measured signal is observed: a sharp peak on the heat source in the heating step is due to the conduction of heat directly from the wire to the surface of the specimen. Conversely, a lower peak and more distributed thermal signal

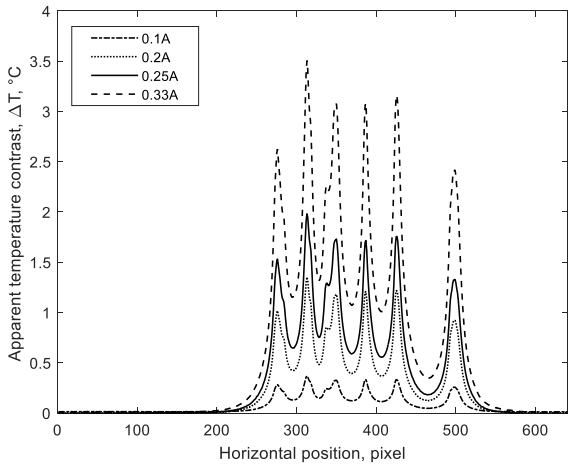

Fig. 14. Distribution of temperature difference in the undamaged T-joint specimen with input current of 0.1 A, 0.2 A, 0.25 A and 0.33 A per SMA wire.

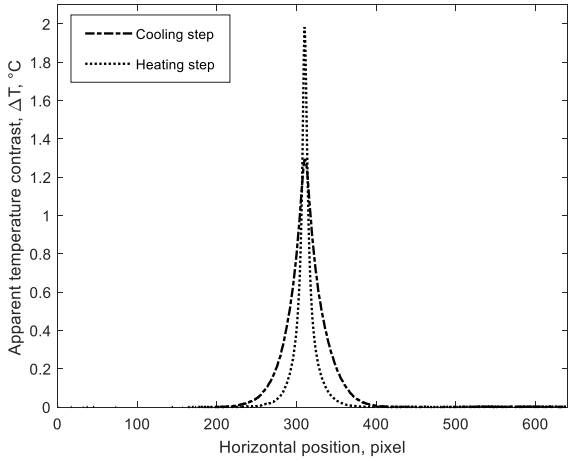

Fig. 15. Distribution of temperature difference observed from the heating and cooling steps in a single SMA wire at 0.25 A.

was perceived from the cooling step due to the dissipation of the heat across the specimen.

An illustration of the SMA tufts position and the corresponding delaminated region before and during the heating process are shown in Fig. 16. SMAs were heated with 0.25 A of electrical current each, whilst the temperature difference for the heating and cooling steps are shown in Figs. 15 and 16. Similar to Fig. 15, during the heating step, SMA wires in the non-delaminated region showed sharp peaks in ΔT (Fig. 17), whereas very low signals were seen from the wires in the delaminated region (Fig. 18). However, the opposite was observed in the cooling step: low thermal signals were seen from the undamaged wires, whilst a higher heat signal was seen from the damaged region. This phenomenon suggests that the gap in delamination allowed heat to dissipate, resulting in less heat conducted to the surface of the composite during heating compared to the undamaged area. During cooling, instead, the retained heat was transferred from the delamination into the surface of the composite, whilst heat from the wires were dissipated by conduction with the bulk of the T-joint.

PCA was applied to the raw thermal data to further improve the acquired thermal contrast. The positions of the undamaged (first and second) and damaged (third to sixth) wires are highlighted by blue triangles in sub-figures of Fig. 19. In the unheated PCA figure, there are no noticeable traces of variation in intensity, suggesting that the five used unheated images are consistent [Fig. 19(a)]. The PCA of the heating process showed obvious signs of intensity change in the first and second SMA tufts, with traces of the third wire [Fig. 19(b)]. No signs of variation were seen from the fourth to sixth wires during the heating process. During the cooling process, significant variation was observed around the first and second wires, less around the third, and only traces around the remaining tufts [Fig. 19(c)]. To illustrate the change in variation

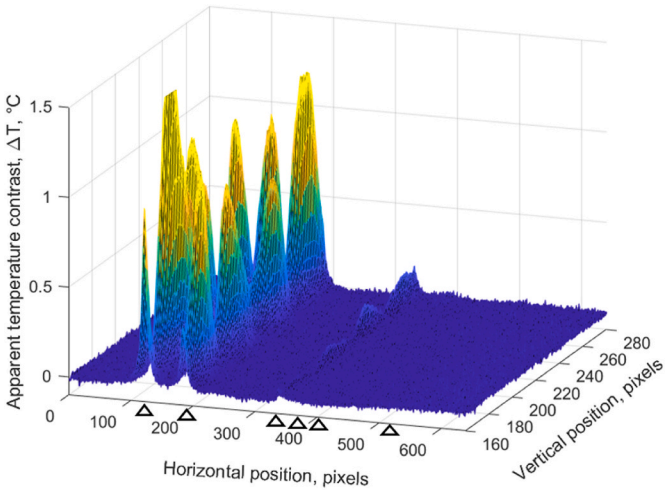

Fig. 17. Distribution of temperature difference on the specimen surface during the heating step. Black triangles illustrate the locations of SMA tufts.

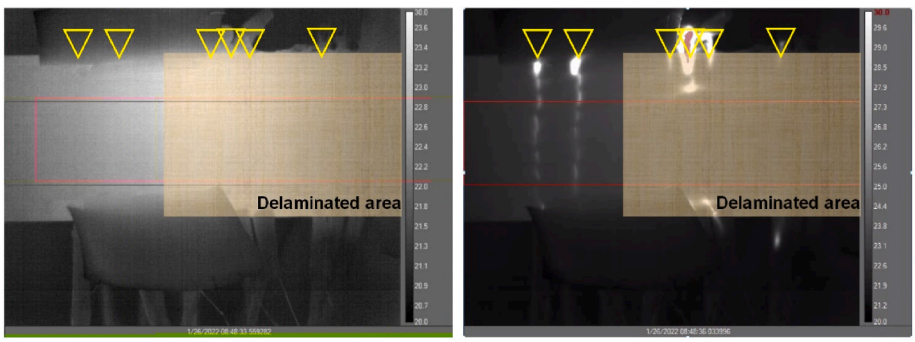

(a) (b)

Fig. 16. Temperature measurements from the composite surface: (a) before heating, and (b) during heating, highlighting the delaminated area. Yellow triangles illustrate the locations of SMA tufts. (For interpretation of the references to colour in this figure legend, the reader is referred to the Web version of this article.)

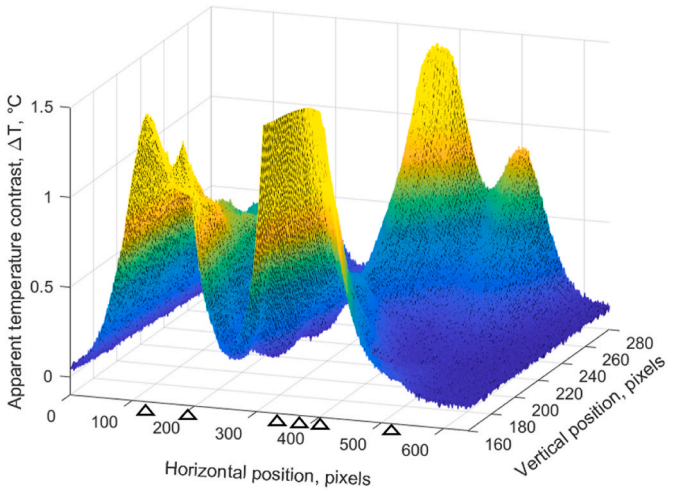

Fig. 18. Distribution of temperature difference on the specimen surface during the cooling step. Black triangles illustrate the locations of SMA tufts.

along the composite T-joint, values from the vertical axes were averaged. Moving average of ten data intervals was plotted to smoothen the curve. Data from the initial state showed some noise with minimal variation and it was plotted for comparison [Fig. 19(d)]. In the heating state, two obvious peaks were seen at the first and second wire positions, corresponding to the wires in the undamaged region. During the cooling process, two high peaks were seen at first and second wire positions (undamaged region), a lower peak on the fourth wire position, and some signals in the sixth wire position (both in the damaged region). This is consistent with observations from the raw intensity data. Results of post-processed thermal images with PCA for damage detection were further validated with optical fractography analysis, as reported in the following section.

3.4. Fractography

Fractographic analysis using optical microscopes was performed on the fracture surfaces of the composite SMA tufted T-joint. Fig. 20 suggests that when the delamination opens during loading, the SMA wires experience the pull-out phenomenon. Tufts were also found to uncoil from the composite [Fig. 20(c)], where matrix-wire debonding and

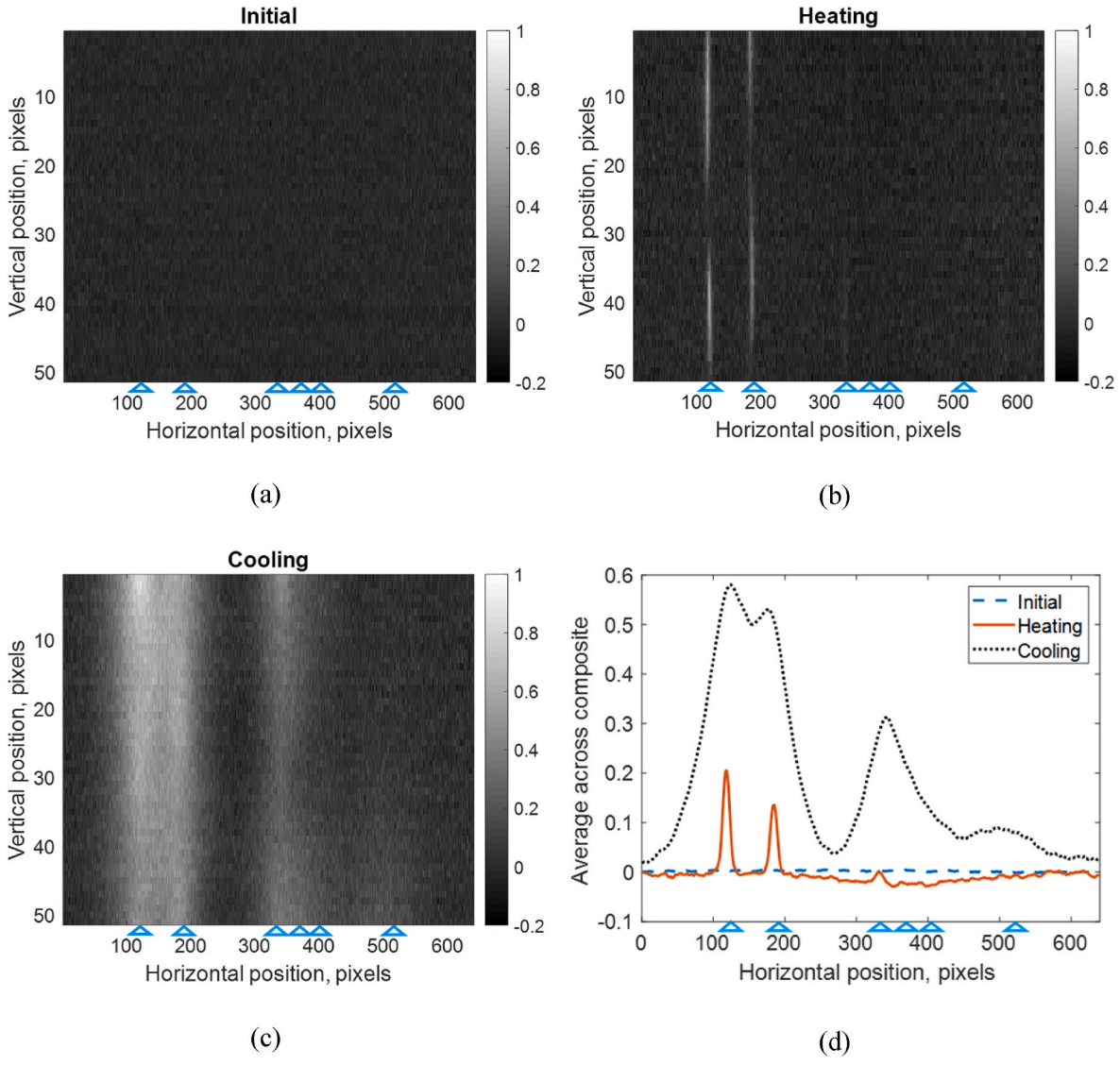

Fig. 19. PCA processed intensity of the composite during the (a) unheated, (b) heating, and (c) cooling process, with indicators for tuft positions. Comparison shown in (d). Blue triangles illustrate the locations of SMA tufts. (For interpretation of the references to colour in this figure legend, the reader is referred to the Web version of this article.)

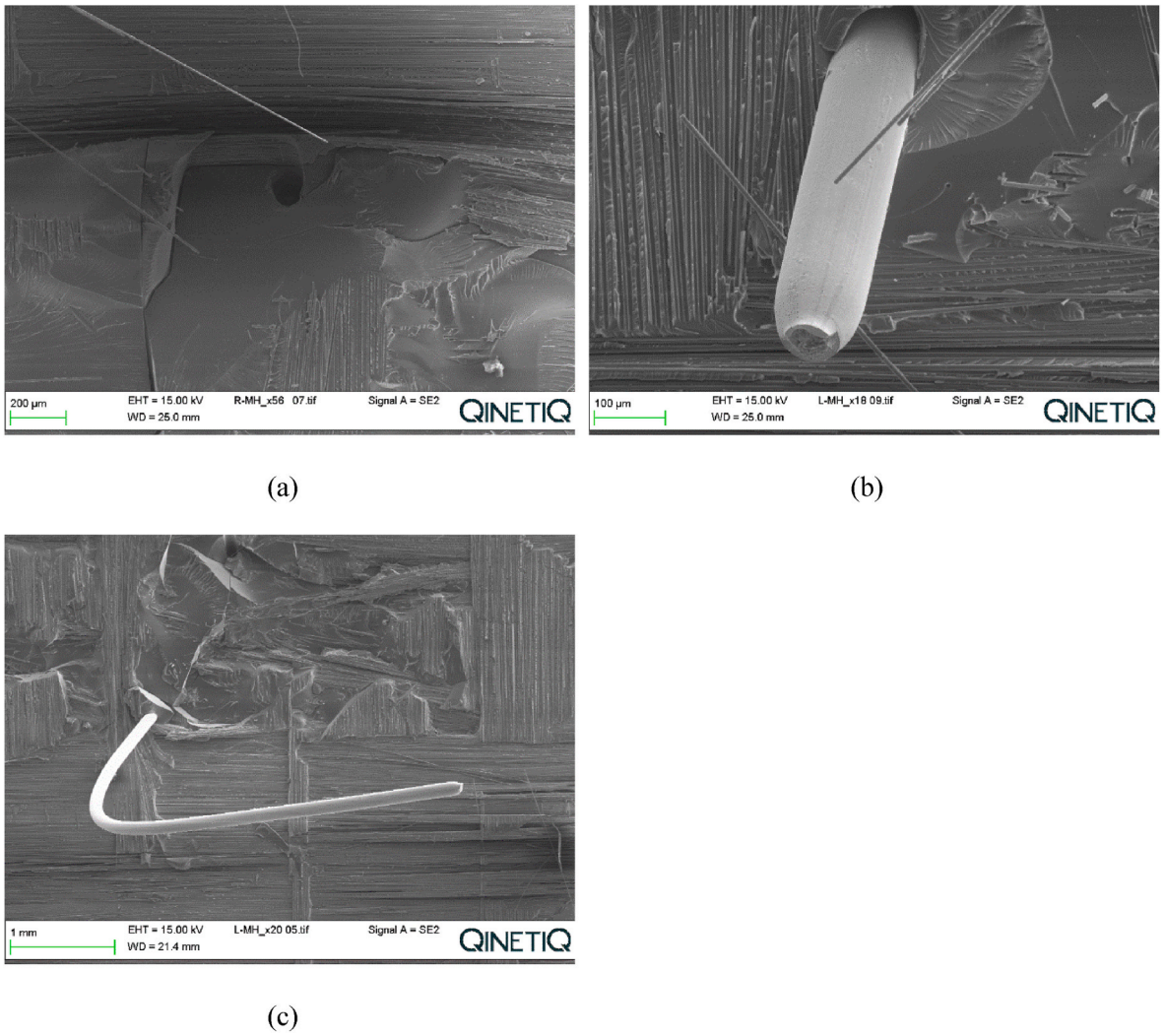

Fig. 20. SEM images of the SMA tufted fracture surface showing (a) hole left by SMA wire pulled through, (b) short strand of SMA wire with ductile tensile fracture, and (c) long strands of SMA wires pulled through the laminate.

breaking of wires were experienced [Fig. 20(b)]. The damage process is described by delamination of the composite and the straining of the SMA, followed by the debonding of the matrix-wire interface and breakage of SMA wires. This explains the observations in the heating and cooling steps for material-enabled thermography reported in the previous Section. During the heating step, good contact was maintained between the wires and composite, allowing good heat conduction to the surface of the material and thus higher heat signal. In the delaminated region, the slipping of the wire due to matrix-wire debonding resulted in a less efficient heat transfer, hence a lower heat signal was observed. During the cooling step, the good contact in the undamaged region had better conduction, and thus retained less heat from the heating step. The debonding damage and delamination space retained heat from the heating step, dissipating during the cooling step and resulting in a higher thermal signal.

4. Conclusions

SMA tuft reinforcements in composite T-joints were used to generate material-enabled strain sensing and NDE thermography. A linear relationship was observed between the SMA wire resistance and delamination opening. Beyond the linear region, damage in SMAs or in the matrix-wire interface have shown to alter the constraint of the wire, thus resulting in inconsistent resistance measurements. Simultaneous resistance measurements from embedded SMA wires have shown to give a good prediction of the delamination across the composite.

Heating of the SMA wires by electrical current produced thermal signals for IR thermographic analysis. The heat signal detected by the IR camera rose with the increase of electrical current in the SMA wires. In the region with no damage, the heating step showed a distinct peak at the heat source; a flatter peak was seen instead in the cooling step. In the delaminated region, low heat signals were observed during the heating step whereas a higher heat signal was found during the cooling step, when compared to the undamaged region. The debonding and delamination reduced the heat conduction during the heating step, retaining heat and releasing it during the cooling step. Processing the heat intensity data by PCA have proved to enhance defect detection. Experimental observations suggested the practicability of SMA tufts for damage detection in composite joints.

Author statement

Weeliam Khor: Conceptualization, Methodology, Investigation, Writing- Original draft preparation.
Anil R. Ravindran: Methodology, Software, Investigation, Writing-Original draft preparation.
Raj B. Ladani: Conceptualization, Supervision, Formal Analysis, Writing - Review & Editing.

Manatsawee Limprapuwiwattana: Investigation, Formal Analysis, Writing- Original draft preparation.
Pete Whitton: Investigation, Validation, Writing- Original draft preparation.
Charlotte Meeks: Formal Analysis, Investigation, Validation, Writing- Original draft preparation.
Andrew D. Foreman: Supervision, Conceptualization, Writing - Review & Editing.
Francesco Ciampa: Supervision, Conceptualization, Formal Analysis, Resources, Writing- Original draft preparation, Funding acquisition.

Declaration of competing interest

The authors declare that they have no known competing financial interests or personal relationships that could have appeared to influence the work reported in this paper.

Data availability

The authors do not have permission to share data.

5 Acknowledgements

Authors are grateful to the Defence Science and Technology Laboratory (DSTL), via the Defence and Security Accelerator (DASA) under the Joint Effort themed call (project contract number ACC6013531). The support of Kevin Denham from DSTL is acknowledged.

Appendix A. Supplementary data

Supplementary data to this article can be found online at https://doi.org/10.1016/j.ndteint.2023.103002.

References

[1] Zeinedini A, Moradi MH, Taghibeigi H, Jamali J. On the mixed mode I/II/III translaminar fracture toughness of cotton/epoxy laminated composites. Theor Appl Fract Mech 2020/10/01/2020;109:102760. https://doi.org/10.1016/j.tafmec.2020.102760.
[2] Sun Q, et al. Failure criteria of unidirectional carbon fiber reinforced polymer composites informed by a computational micromechanics model. Compos Sci Technol 2019;172:81–95. https://doi.org/10.1016/j.compscitech.2019.01.012.
[3] Laffan MJ. Development of translaminar fracture toughness testing methods for composite materials. Doctor of Philosophy (PhD), Aeronautics, Imperial College London, Imperial College London. 2012 [Online]. Available: http://hdl.handle.net/10044/1/9659.
[4] Laffan MJ. 5 - testing the toughness of polymer matrix composites. In: Robinson P, Greenhalgh E, Pinho S, editors. Failure mechanisms in polymer matrix composites. Woodhead Publishing; 2012. p. 110–28.
[5] J. P. Reis, M. de Moura, and S. Samborski, "Thermoplastic composites and their promising applications in joining and repair composites structures: a review," Materials, vol. 13, no. 24, doi: 10.3390/ma13245832.
[6] Kazemianfar B, Nami MR. Can a 3D woven GFRP composite really provide better impact resistance compared to a 2D woven GFRP composite at all of the thicknesses? Structures 2022;35:36–45. https://doi.org/10.1016/j.istruc.2021.10.091.
[7] Bianchi F, Koh TM, Zhang X, Partridge IK, Mouritz AP. Finite element modelling of z-pinned composite T-joints. Compos Sci Technol 2012;73:48–56. https://doi.org/10.1016/j.compscitech.2012.09.008.
[8] Cartié DDR, Dell'Anno G, Poulin E, Partridge IK. 3D reinforcement of stiffener-to-skin T-joints by Z-pinning and tufting. Eng Fract Mech 2006;73(16):2532–40. https://doi.org/10.1016/j.engfracmech.2006.06.012.
[9] Dell'Anno G, Treiber JWG, Partridge IK. Manufacturing of composite parts reinforced through-thickness by tufting. Robot Comput Integrated Manuf 2016;37:262–72. https://doi.org/10.1016/j.rcim.2015.04.004.
[10] Dell'Anno G, et al. Automated manufacture of 3D reinforced aerospace composite structures. Int J Struct Integr 2012;3(1):22–40. https://doi.org/10.1108/17579861211209975.
[11] Treiber JWG, Cartié DDR, Partridge IK. Determination of crack bridging laws in tufted composites. In: Presented at the ICCM international conferences on composite materials; 2009.
[12] Scott M, Dell'Anno G, Clegg H. Effect of process parameters on the geometry of composite parts reinforced by through-the-thickness tufting. Appl Compos Mater 2018;25(4):785–96. https://doi.org/10.1007/s10443-018-9710-4.
[13] Colin de Verdiere M, Skordos AA, Walton AC, May M. Influence of loading rate on the delamination response of untufted and tufted carbon epoxy non-crimp fabric composites/Mode II. Eng Fract Mech 2012;96:1–10. https://doi.org/10.1016/j.engfracmech.2011.12.011.
[14] Lombetti DM, Skordos AA. Lightning strike and delamination performance of metal tufted carbon composites. Compos Struct 2019;209:694–9. https://doi.org/10.1016/j.compstruct.2018.11.005.
[15] Bhaskar J, Kumar Sharma A, Bhattacharya B, Adhikari S. A review on shape memory alloy reinforced polymer composite materials and structures. Smart Mater Struct 2020;29(7):073001. https://doi.org/10.1088/1361-665x/ab8836.
[16] Cherkaoui M, Sun QP, Song GQ. Micromechanics modeling of composite with ductile matrix and shape memory alloy reinforcement. Int J Solid Struct 2000;37(11):1577–94. https://doi.org/10.1016/S0020-7683(98)00332-1.
[17] Cohades A, Michaud V. Shape memory alloys in fibre-reinforced polymer composites. Adv Ind Eng Polym Res 2018;1(1):66–81. https://doi.org/10.1016/j.aiepr.2018.07.001.
[18] A. Dębska, P. Gwoździewicz, A. Seruga, X. Balandraud, and J.-F. Destrebecq, "The application of Ni–Ti SMA wires in the external prestressing of concrete hollow cylinders," Materials, vol. 14, no. 6, doi: 10.3390/ma14061354.
[19] Coduri M, Lausi A, Tuissi A. The high performance shape memory effect (HP-SME) in Ni rich NiTi wires: in situ X-ray diffraction on thermal cycling. 10.1051/matecconf/20153303008 MATEC Web Conf 2015;33. https://doi.org/10.1051/matecconf/20153303008.
[20] Ciampa F, et al. Shape memory alloy tufted composites combining high delamination resistant and crack closure properties. Compos Appl Sci Manuf 2021:106455. https://doi.org/10.1016/j.compositesa.2021.106455.
[21] Khor W, et al. Improving the damage tolerance of composite T-joints using shape memory alloy tufts. Compos Appl Sci Manuf 2023;168:107474. https://doi.org/10.1016/j.compositesa.2023.107474.
[22] Wang J, Lu C, Zhang K. Textile-based strain sensor for human motion detection. Energy Environ Mater 2020;3(1):80–100. https://doi.org/10.1002/eem2.12041.
[23] Wu S, et al. Novel electrically conductive porous PDMS/carbon nanofiber composites for deformable strain sensors and conductors. ACS Appl Mater Interfaces 2017;9(16):14207–15. https://doi.org/10.1021/acsami.7b00847.
[24] Li Y-Q, Huang P, Zhu W-B, Fu S-Y, Hu N, Liao K. Flexible wire-shaped strain sensor from cotton thread for human health and motion detection. Sci Rep 2017;7(1):45013. https://doi.org/10.1038/srep45013.
[25] liu H, Jiang H, Du F, Zhang D, Li Z, Zhou H. Flexible and degradable paper-based strain sensor with low cost. ACS Sustainable Chem Eng 2017;5(11):10538–43. https://doi.org/10.1021/acssuschemeng.7b02540.
[26] Chossat JB, Yiwei T, Duchaine V, Park YL. Wearable soft artificial skin for hand motion detection with embedded microfluidic strain sensing. In: 2015 IEEE international conference on robotics and automation (ICRA), 26-30 may 2015; 2015. p. 2568–73. https://doi.org/10.1109/ICRA.2015.7139544.
[27] Saleh MA, Kempers R, Melenka GW. 3D printed continuous wire polymer composites strain sensors for structural health monitoring. Smart Mater Struct 2019;28(10):105041. https://doi.org/10.1088/1361-665x/aafdef.
[28] Li X, Levy C, Elaadil L. Multiwalled carbon nanotube film for strain sensing. Nanotechnology 2008;19(4):045501. https://doi.org/10.1088/0957-4484/19/04/045501.
[29] Furst SJ, Crews JH, Seelecke S. Stress, strain, and resistance behavior of two opposing shape memory alloy actuator wires for resistance-based self-sensing applications. J Intell Mater Syst Struct 2013;24(16):1951–68. https://doi.org/10.1177/1045389X13486715.
[30] Cui D, Song G, Li H. Modeling of the electrical resistance of shape memory alloy wires. Smart Mater Struct 2010;19(5):055019. https://doi.org/10.1088/0964-1726/19/5/055019.
[31] Nagai H, Oishi R. Shape memory alloys as strain sensors in composites. Smart Mater Struct 2006;15(2):493–8. https://doi.org/10.1088/0964-1726/15/2/032.
[32] Abot JL, Schulz MJ, Song Y, Medikonda S, Rooy N. Novel distributed strain sensing in polymeric materials. Smart Mater Struct 2010;19(8):085007. https://doi.org/10.1088/0964-1726/19/8/085007.
[33] Thierry V, Mesnil O, Chronopoulos D. Experimental and numerical determination of the wave dispersion characteristics of complex 3D woven composites. Ultrasonics 2020;103:106068. https://doi.org/10.1016/j.ultras.2020.106068.
[34] Pinto F, Maroun FY, Meo M. Material enabled thermography. NDT E Int 2014;67:1–9. https://doi.org/10.1016/j.ndteint.2014.06.004.
[35] Tomita K, Chew MYL. A review of infrared thermography for delamination detection on infrastructures and buildings. Sensors 2022;22(2):423. https://www.mdpi.com/1424-8220/22/2/423.
[36] Chun Pj, Hayashi S. Development of a concrete floating and delamination detection system using infrared thermography. IEEE ASME Trans Mechatron 2021;26(6):2835–44. https://doi.org/10.1109/TMECH.2021.3106867.
[37] Cotič P, Kolarič D, Bosiljkov VB, Bosiljkov V, Jagličić Z. Determination of the applicability and limits of void and delamination detection in concrete structures using infrared thermography. NDT E Int 2015;74:87–93. https://doi.org/10.1016/j.ndteint.2015.05.003.
[38] Badghaish AA, Fleming DC. Non-destructive inspection of composites using step heating thermography. J Compos Mater 2008;42(13):1337–57. https://doi.org/10.1177/0021998308092202.
[39] Wang Z, Tian G, Meo M, Ciampa F. Image processing based quantitative damage evaluation in composites with long pulse thermography. NDT E Int 2018;99:93–104. https://doi.org/10.1016/j.ndteint.2018.07.004.
[40] Ghadermazi K, Khozeimeh MA, Taheri-Behrooz F, Safizadeh MS. Delamination detection in glass–epoxy composites using step-phase thermography (SPT).

Infrared Phys Technol 2015;72:204–9. https://doi.org/10.1016/j.infrared.2015.08.006.
[41] Cheng L, Tian GY. Comparison of nondestructive testing methods on detection of delaminations in composites. J Sens 2012;2012:408437. https://doi.org/10.1155/2012/408437.
[42] Zeng Z, Li C, Tao N, Feng L, Zhang C. Depth prediction of non-air interface defect using pulsed thermography. NDT E Int 2012;48:39–45. https://doi.org/10.1016/j.ndteint.2012.02.008.
[43] Montanini R, Freni F. Non-destructive evaluation of thick glass fiber-reinforced composites by means of optically excited lock-in thermography. Compos Appl Sci Manuf 2012;43(11):2075–82. https://doi.org/10.1016/j.compositesa.2012.06.004.
[44] Avdelidis NP, Hawtin BC, Almond DP. Transient thermography in the assessment of defects of aircraft composites. NDT E Int 2003;36(6):433–9. https://doi.org/10.1016/S0963-8695(03)00052-5.
[45] Ciampa F, Mahmoodi P, Pinto F, Meo M. Recent advances in active infrared thermography for non-destructive testing of aerospace components. Sensors 2018;18(2):609 [Online]. Available: https://www.mdpi.com/1424-8220/18/2/609.
[46] Angioni SL, Ciampa F, Pinto F, Scarselli G, Almond DP, Meo M. An analytical model for defect depth estimation using pulsed thermography. Exp Mech 2016;56(6):1111–22. https://doi.org/10.1007/s11340-016-0143-4.
[47] Grammatikos SA, Kordatos EZ, Matikas TE, David C, Paipetis AS. Current injection phase thermography for low-velocity impact damage identification in composite laminates. Mater Des 2014;55:429–41. https://doi.org/10.1016/j.matdes.2013.09.019.
[48] Galos J, Hu Y, Ravindran AR, Ladani RB, Mouritz AP. Electrical properties of 3D printed continuous carbon fibre composites made using the FDM process. Compos Appl Sci Manuf 2021;151:106661. https://doi.org/10.1016/j.compositesa.2021.106661.
[49] Wang Z, Wan L, Xiong N, Zhu J, Ciampa F. Variational level set and fuzzy clustering for enhanced thermal image segmentation and damage assessment. NDT E Int 2021;118:102396. https://doi.org/10.1016/j.ndteint.2020.102396.
[50] Jolliffe IT, Cadima J. Principal component analysis: a review and recent developments. Phil Trans Math Phys Eng Sci 2016;374(2065):20150202. https://doi.org/10.1098/rsta.2015.0202.
[51] Jolliffe IT. Principal component analysis (springer series in statistics). New York, NY: Springer; 2002. p. 488.
[52] Vaijapurkar VB, Ravinder Y. Electrical resistance modeling of shape memory alloy wire using an efficient performance analysis approach. Shape Memory Superelasticity 2022;8(2):168–82. https://doi.org/10.1007/s40830-022-00369-y.